



Contents lists available at ScienceDirect

## Journal of the Mechanics and Physics of Solids

journal homepage: [www.elsevier.com/locate/jmps](http://www.elsevier.com/locate/jmps)

# Microstructural evolution and failure in short fiber soft composites: Experiments and modeling

Chengyang Mo<sup>a</sup>, Yijie Jiang<sup>a,b</sup>, Jordan R. Raney<sup>a,\*</sup><sup>a</sup> Department of Mechanical Engineering and Applied Mechanics, University of Pennsylvania, Philadelphia, PA, 19014, USA<sup>b</sup> Department of Mechanical and Energy Engineering, University of North Texas, Denton, TX, 76207, USA

## ARTICLE INFO

## Article history:

Received 11 January 2020

Revised 19 March 2020

Accepted 13 April 2020

Available online 21 April 2020

## Keywords:

Composites

Failure

Soft materials

## ABSTRACT

In this work, we systematically study the mechanics of short glass fiber composites with a soft, hyperelastic matrix (polydimethylsiloxane). The fiber orientation can be controlled by fabricating the materials with direct ink writing, an extrusion-based 3D printing method. We specifically characterize the damage evolution in these materials when subject to tensile and cyclic loading by developing a micromechanical model, a continuum model, and by performing experiments. The stress-stretch behavior and damage evolution are highly-dependent on both volume fraction and fiber orientation. We focus primarily on loading that is parallel with the fiber alignment, which shows rich complexities as a function of volume fraction, including variable softening and non-monotonic increase of the yield strength. Unlike most prior work, we use *in situ* optical measurements and digital image correlation during mechanical loading to quantify the highly-nonhomogeneous stretch field at macroscopic and microscopic length scales, and to simultaneously visualize the mechanisms underlying the damage evolution and complexities in the stress-stretch response, namely fiber-matrix debonding. The micromechanical model is based on modifications to the classic shear lag model, which include incorporation of fiber length distribution as a function of volume fraction and use of Weibull distributions to account for the probability of fiber-matrix debonding. The continuum model is based on hyperelastic strain energy with damage parameters for both matrix and fibers. The combination of the two models is able to capture the stress-stretch behavior and damage evolution well, and also the Mullins-like, history-dependent cyclic loading behavior we observe in experiments.

© 2020 Elsevier Ltd. All rights reserved.

\* Corresponding author.

E-mail address: [raney@seas.upenn.edu](mailto:raney@seas.upenn.edu) (J.R. Raney).

## Contents

1. Introduction	2
2. Materials and methods	3
2.1. 3D printing short fiber composites	3
2.2. Experimental setup	3
3. Experimental results	4
3.1. Stress-stretch response of tensile specimens	4
3.2. Macroscale in situ optical characterization	5
3.3. In situ microstructural characterization	7
4. Modeling	7
4.1. Micromechanical model	7
4.2. Constitutive model	10
5. Discussion	11
5.1. Micromechanical model results	11
5.2. Constitutive model results	13
6. Conclusion	16
Declaration of Competing Interest	17
CRedit authorship contribution statement	17
Acknowledgments	17
References	17

## 1. Introduction

Short fiber composites have been the focus of research interest for many decades for their excellent combination of mechanical properties, such as strength and stiffness, and their mass efficiency (Compton and Lewis, 2014). While structural composites have been a focus of much of this effort, often motivated by natural materials such as wood (Marklund and Varna, 2009), teeth (Bechtel et al., 2010), and marine shells (Weaver et al., 2012), understanding the mechanical behavior of short fiber composites with soft matrices is of vital importance. These materials are ubiquitous in biological materials, such as arterial wall (Gasser et al., 2006), collagen networks (Bircher et al., 2019), skin (Yang et al., 2015), and other tissues. The anisotropy of the fibers produces complex localized toughening and failure characteristics which are crucial in determining failure in these biological systems, and additionally play a key role in understanding pathologies (De Vita and Slaughter, 2007). Soft composites are also of growing interest for applications as smart materials and in soft robotics, where fiber anisotropy can be used to control pneumatic actuation (Kim et al., 2019), shape morphing (Boley et al., 2019; Gladman et al., 2016), and embodying logic, sensing, and actuation (Jiang et al., 2019). Advances in additive manufacturing now allow the production of free-form structures from short fiber-reinforced polymers via 3D printers (Compton and Lewis, 2014; Jiang et al., 2019; Raney et al., 2018; Raney and Lewis, 2015; Zhong et al., 2001). These techniques allow spatial control of fiber orientation (Jiang et al., 2019; Raney et al., 2018), raising the prospect of facile fabrication of complex heterogeneous composites. However, the lack of experimental methods for quantifying the microstructural evolution leading up to and during failure has limited the understanding of these composites (Koh et al., 2013; Li, 2016; Peña, 2011).

Numerous studies have offered insight into failure mechanisms of fiber-reinforced soft composites under a variety of loading conditions by using continuum modeling (phenomenological), micromechanical modeling (mechanistic), numerical methods, and experimental approaches. An early continuum model dealing with plasticity and failure of fiber composites was proposed by Triantafyllidis and Abeyaratne (Triantafyllidis and Abeyaratne, 1983) based on Blatz-Ko material. Assuming perfect bonding between fibers and matrix, they showed that when composites are compressed parallel to and pulled perpendicular to the direction of fiber alignment that the material can experience instability in the form of a loss of ellipticity, also called fiber kinking. This model was further developed (Budiansky and Fleck, 1993; Jensen and Christoffersen, 1997) to predict the onset of fiber kinking for finite fiber stiffness. Qiu and Pence studied such effects within an incompressible matrix using a Neo-Hookean formulation (Qiu and Pence, 1997a, 1997b), while Merodio and Ogden further improved the model for Neo-Hookean materials by considering various reinforcement formulations (Merodio and Ogden, 2002, 2005a, 2005b). Phenomenological models have been effective for predicting mechanical behaviors such as strain hardening in rubber and fiber damage in biological tissues. Continuum models have also been developed to explain stretch-induced softening in elastomers (Mullins effect (Mullins, 1947)) by taking into account the polymer chain lengths in the constitutive formulation (Qi and Boyce, 2004). Continuum models with an anisotropic damage parameter to the fiber reinforcement were proposed by Simo (Simo, 1987) to successfully predict the mechanical response of soft biological tissues with a damage history

(Li, 2016; Peña, 2011). These models have been applied to tendons (De Vita and Slaughter, 2007) and blood vessel walls (Marini et al., 2012; Volokh, 2008), and have been experimentally verified.

The specific failure mechanisms of fiber-matrix composites have been considered via micromechanical models. The shear lag model (Ghassemieh and Nassehi, 2001; Hull and Clyne, 1996) accounts for the geometry of the fibers, with the assumption that the load is transferred from the matrix to the fiber via shear stresses. The distribution of shear stress along the fibers can be calculated from this model. The available shear stress distributions allow introduction of a damage criterion to describe the failure characteristics. A 2D shear lag simulation was developed to investigate interfacial debonding between fibers and matrix (Ochiai et al., 1999), with the debonding process based on shear stress and energy release rate criteria. Numerical methods have also been employed to study failure of fiber composites. For example, debonding of continuous carbon fibers in a soft hyperelastic matrix has been investigated using finite element models to explain the nonlinear behavior and softening during loading perpendicular to the fiber direction (López Jiménez and Pellegrino, 2012).

Despite these many efforts at capturing failure behavior in soft composites, progress in understanding the mechanisms of material failure has been greatly inhibited by the difficulty of experimentally visualizing the multiscale structural changes during and leading up to failure, a point repeatedly recognized by prior researchers of fibrous systems (Koh et al., 2013; Li, 2016; Peña, 2011). Non-destructive methods such as Raman spectroscopy (Melanitis et al., 1993) and photoelasticity (Tsai and Kim, 1996) have been used to understand the stress state around single fibers embedded in a matrix during uniaxial loading and fiber pullout, respectively. Fiber networks have been studied experimentally (Bircher et al., 2019; Koh et al., 2013; Yang et al., 2015) using X-Ray scattering (Yang et al., 2015), optical microscopy, electron microscopy (Bircher et al., 2019; Koh et al., 2013), and light scattering (Sacks, 2003) during stretching to relate fiber reorientation to strain stiffening and damage evolution. In metallic alloys it has proven effective to use *in situ* techniques such as digital image correlation (DIC) and electron microscopy to quantify localized deformation and micromechanical damage during loading, e.g., in Cu-Al alloys (Ranc and Wagner, 2005; Yilmaz, 2011), steel (Zavattieri et al., 2009), and magnesium alloys (Mo and Kontsos, 2018). However, there are a lack of reported experimental data that measure microstructural changes in short fiber composites and that bridge the relevant length scales from the fiber-matrix interactions and local deformation to the non-homogeneous macroscopic deformation leading up to failure.

In this paper, we present a systematic study of mechanical properties and failure processes in 3D printed polydimethylsiloxane (PDMS)-glass fiber (GF) composites, with the fiber orientation controlled via the printing process. Using *in situ* optical imaging of the microstructure to measure damage and DIC to quantify deformation at multiple length scales during loading, we experimentally study the damage process and its effect on mechanical properties. Additionally, we develop two models that agree well with the experimental observations, including i) a micromechanical stress-based model using a modified shear lag model and ii) a constitutive energy-based model using a damage parameter.

## 2. Materials and methods

### 2.1. 3D printing short fiber composites

We 3D print PDMS reinforced with short glass fibers (GF) using direct ink writing (DIW). Dow Corning SE 1700 (1:10 crosslinker ratio) and Dow Corning Sylgard 184 (1:10 crosslinker ratio) are mixed under vacuum in a ratio of 85:15 wt.%, with milled glass fibers (Fiber Glast 29) added. The volume fraction of glass fibers ranges from 3% to 12% in this study. Subsequently the material is transferred to a syringe and centrifuged to remove air. As is typical for DIW processes (Lewis, 2006; Raney and Lewis, 2015), the material is rheologically tuned to possess a viscoelastic yield stress, allowing it to flow freely through an extrusion nozzle but to hold its shape after extrusion (see rheological characterization for this material in our previous work (Jiang et al., 2019)). The material is extruded through a 410  $\mu\text{m}$  nozzle, with the flow controlled pneumatically. We print tensile specimens with a thickness of 4 layers ( $\sim 1.2$  mm, due to interlayer spacing less than the nozzle diameter). Due to the shear stress in the nozzle during extrusion (Compton and Lewis, 2014; Gladman et al., 2016; Jiang et al., 2019; Malek et al., 2017; Raney et al., 2018) the fiber orientation in the tensile specimens can be controlled by the print path. We define the angle  $\phi$  as the angle between this predominant fiber orientation and the loading direction (shown in Fig. 1(a)). When  $\phi = 0^\circ$ , loading is parallel to the fiber direction, conventionally referred to as loading in the longitudinal direction. When  $\phi = 90^\circ$ , loading is perpendicular to the fiber direction, conventionally referred to as transverse loading. A microscope image of a printed specimen is shown in Fig. 1(b), showing the fibers aligned along the print direction. Lengths of individual fibers are measured from the microscope images using ImageJ's measurement features. Dozens of fibers are measured for each volume fraction to characterize the fiber length distribution. Sample distributions for 3% and 5% volume fraction are shown in Fig. 1(c).

### 2.2. Experimental setup

Two types of tensile tests are conducted in this study: one for characterizing macroscale deformation and the other for characterizing microscale deformation, at approximately the length scale of the fibers themselves. In both cases, deformation is monitored optically, via a high-resolution camera or a microscope, respectively, to allow measurement of the local deformation field via digital image correlation (DIC).



**Fig. 1.** (a) Schematic of the direct ink writing process. The angle  $\phi$  indicates the angle between the loading direction and the predominant fiber orientation. (b) Representative optical image showing aligned fibers in the printed sample. (c) Fiber length distribution for 3% and 5% volume fraction samples.

Macroscale tensile testing is conducted with a commercial materials test system (Instron Model 5564) operating under displacement control at a strain rate of  $0.02 \text{ s}^{-1}$  and tested to failure. Samples are gripped with a pneumatic grip at a pressure of 25 psi. Microscale testing is conducted with a customized screw driven desktop device. This more compact test fixture allows stretch of up to 1.25 to be applied to specimens while they are under an optical microscope (Keyence VH-5000) at 100x magnification. A polarizer is mounted to avoid strong reflection from the top surface of our samples. With this fixture, stretch can be applied at one of seven evenly-spaced intervals, giving a minimum stretch interval of  $\sim 0.035$ . The goal of the microscale testing is to reveal the relationship between microstructure (including information such as local fiber orientation and degree of debonding) and the local deformation, which is measured via DIC.

To perform DIC, speckles with an approximate size of  $10 \mu\text{m}$  are first applied on the surfaces of the specimens using an airbrush. For macroscale testing, videos are recorded at 4K resolution (resolving pixel size of  $14 \mu\text{m}/\text{pixel}$ ) with a recording rate of 24 frames per second. DIC is conducted by extracting frames at 2 frames per second with subset size of 12 pixels and subset spacing of 6 pixels. Due to the extremely fine size of the speckles the same pattern can be used for DIC in microscale testing. For the microscale testing a microscope image is captured after each increment of stretch is applied. This enables tracking of the deformation via the speckles while microstructural changes, such as fiber orientation and (if relevant) fiber debonding, are simultaneously observed via the same micrographs. Images are captured at  $2.25 \mu\text{m}/\text{pixel}$ . DIC is conducted on the captured images with subset size of 40 pixels and subset spacing of 10 pixels. Strain for both scales is calculated with a window of 5 subsets. For both length scales, DIC is performed using the open source Ncorr package with MATLAB (Blaber et al., 2015).

### 3. Experimental results

#### 3.1. Stress-stretch response of tensile specimens

As expected for fiber composites, the mechanical properties are highly-dependent on the angle of loading relative to the fiber orientation. Fig. 2(a) shows the experimental stress-stretch curves as a function of fiber orientation  $\phi$  for a printed PDMS-glass fiber composite with 5 vol.% glass fibers. The initial elastic moduli ( $E_{11}$ ) can be extracted from these curves (close to  $\lambda = 1$ ), as shown in Fig. 2(b), revealing that a longitudinal fiber orientation ( $\phi = 0^\circ$ ) produces an initial modulus roughly five times higher than a transverse fiber orientation ( $\phi = 90^\circ$ ), even for this modest quantity of fibers. The variation in initial modulus as a function of orientation agrees well with classic predictions for short fiber composites (Lees, 1968). More interestingly, the shape of the stress-stretch curve depends on the orientation. When the fibers are aligned in the loading direction the sample exhibits yielding and softening. In contrast, when the fibers are perpendicular to the loading direction no comparable yielding event is observed.

Interestingly, variations in the fiber volume fraction can lead to a similar transition. Fig. 3(a) shows three stress-stretch curves representative of specimens with longitudinal fiber orientation ( $\phi = 0^\circ$ ) and, respectively, 3 vol.%, 5 vol.%, and 10 vol.%. For lower volume fractions (3 vol.% and 5 vol.%), the material exhibits significant ductility (reaching rupture stretch of  $\lambda_R > 3$  and  $\lambda_R > 2$  for 3 vol.% and 5 vol.%, respectively). In this case the material initially deforms nominally linearly with high modulus, and subsequently exhibits significant softening, during which the modulus reaches zero or even negative. Finally, at higher stretch the material once again exhibits increased modulus, but at a modulus lower than the initial modulus. Comparable behavior has been observed in hybrid laminates, in which different layers of the laminate have different compositions of fibers (Selezneva et al., 2018), but not to the best of our knowledge in simple short fiber composites. In contrast with the above, specimens with higher volume fraction (e.g., the 10 vol.% case shown in Fig. 3a) do not show the same complex stress-stretch response, breaking almost immediately as they reach yield strength.

The initial elastic modulus (Fig. 3(b)) shows a monotonic increase as a function of volume fraction, as would be expected since there are more stiff fillers in the composites. However, the trend in ultimate tensile strength (Fig. 3(c)) is counter-intuitive: the tensile strength is significantly higher for the composite with 3 vol.% fibers than for the composite with 5 vol.% fibers. The reason for this is hinted at in Fig. 3(a). In both cases failure occurs at high stretch where the response of the matrix dominates the mechanical behavior; however, in the latter case, the stretch of rupture  $\lambda_R$  is greatly reduced by

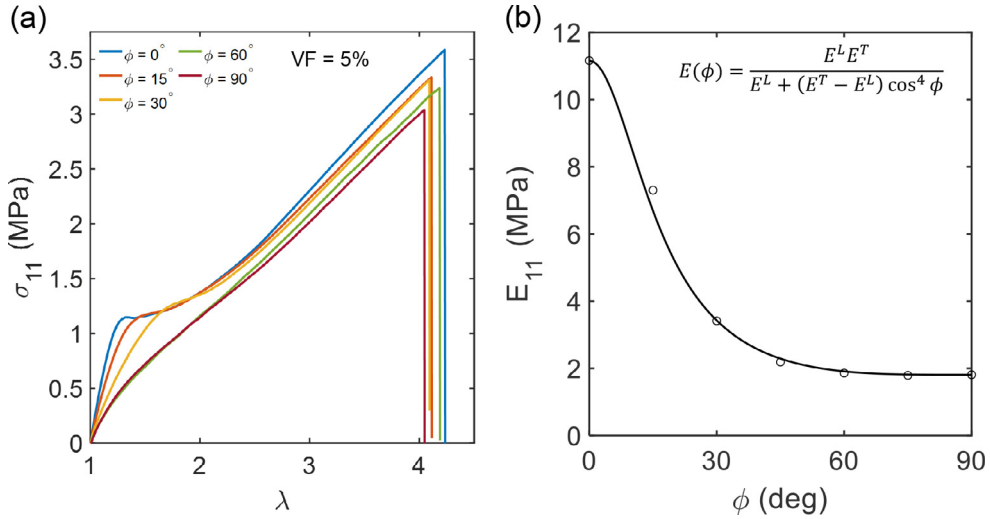


**Fig. 2.** Experimental measurements of PDMS glass fiber composites: Effect of fiber orientation: (a) Stress-stretch response for different loading orientations for specimens with 5 vol.% fibers; (b) Effect of fiber orientation on initial elastic modulus  $E_{11}$ . Solid line is fit according to Lees (Lees, 1968) where  $E^L$  is the modulus for longitudinal samples ( $\phi = 0^\circ$ ) and  $E^T$  is the modulus for transverse samples ( $\phi = 90^\circ$ ).

the increase in the fiber volume fraction. This is clearly shown in Fig. 3(d), where  $\lambda_R$  is plotted as a function of volume fraction, revealing a striking reduction in  $\lambda_R$  between volume fractions of 4–6 vol.%. Composites with a low volume fraction exhibit a high value for  $\lambda_R$ , almost matching that of pure PDMS whose stress and stretch is also plotted in Fig. 3(a), while  $\lambda_R$  for higher volume fraction is consistently low (near 1.35). Because this transition is very abrupt, samples with volume fractions near this transition point (e.g., around 5 vol.%) show large variation in  $\lambda_R$ . This type of behavior can be modeled as a Weibull function in which the two regimes for  $\lambda_R$  correspond to two distinct modes of failure. A Weibull function is fit to the data in Fig. 3(d) (solid line), revealing an excellent agreement with the experimental data. Weibull distributions have been previously used in probabilistic constitutive laws of fibrous materials, e.g., for capturing the contribution of collagen to the stress-stretch behavior in subfailure stretch regimes in ligaments (De Vita and Slaughter, 2007; Guo and De Vita, 2009).

We also characterized the complex stress-stretch response of the lower volume fraction composites under cyclic loading. Fig. 4(a) shows a representative stress-stretch plot for a specimen with 3 vol.% glass fibers when subjected to cyclic loading to increasing stretch values. The stress-stretch behavior is analogous to the Mullins effect observed in rubbers (Mullins, 1947). Initially, prior to softening, the materials exhibit recoverable elastic response. As the deformation continues through the softening region, the loading and unloading clearly exhibits hysteresis and residual stretch. Such variations on the classic Mullins effect have been previously observed experimentally in other materials, such as particle filled rubber (Dorfmann and Ogden, 2004) and carbon nanotube arrays (Blesgen et al., 2013). Fig. 4b shows the initial modulus as a function of the maximum stretch for each loading cycle, giving one measure of the degree of damage in the material. The initial modulus holds nominally constant for the first three loading cycles (indicating minimal damage at small stretch) before undergoing a clear degradation in the initial modulus upon loading to higher stretch, ultimately approaching a value comparable to the modulus of the pure PDMS matrix.

### 3.2. Macroscale *in situ* optical characterization

The Mullins-like cyclic data of Fig. 4 is indicative of a microstructure that is undergoing damage in the stretch-softening portion of the stress-stretch curve. It turns out that this affects the specimen in ways that can be observed macroscopically. We recorded high-resolution images of the surfaces of specimens with 5 vol.% glass fiber during uniaxial stretch. Representative longitudinal ( $\phi = 0^\circ$ ) and transverse ( $\phi = 90^\circ$ ) stress-stretch curves are shown in black and red, respectively, in Fig. 5(a). The images of the samples corresponding to the seven different indicated values of stretch are shown in Fig. 5(b). Initially, the composites are optically transparent for both longitudinal and transverse specimens. However, when stretched beyond  $\lambda = \lambda_2$  the longitudinal samples exhibit an irreversible whitening similar to crazing or other void formation in polymer systems. However, crazing is not usually observed in pure PDMS (typically opacity increases during stretching of PDMS due to thinning of the material (López Jiménez et al., 2016)). The evident whitening first appears locally and subsequently spreads across the rest of the sample ( $\lambda_3$  through  $\lambda_5$ ). Eventually, the entire sample exhibits this change (see  $\lambda_7$ ). The transverse samples, however, do not exhibit comparable whitening, remaining mostly transparent as they are stretched to failure.

The non-homogeneous initiation of whitening in Fig. 5(b) is associated with non-homogeneous deformation, which we quantify via DIC, using the high-resolution images recorded during the tensile test. Fig. 6(a) shows the evolution of the

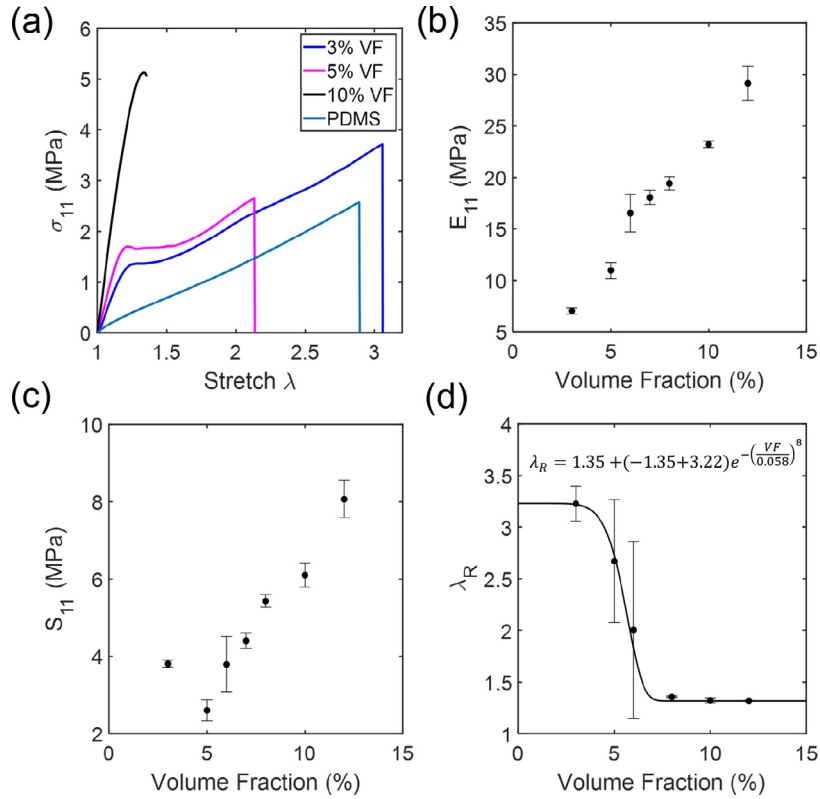


**Fig. 3.** Experimental measurements of PDMS-glass fiber composites: Effect of volume fraction: (a) Stress-stretch response of three different volume fractions; Effect of volume fraction on (b) initial elastic modulus  $E_{11}$ , (c) ultimate tensile strength  $S_{11}$  and (d) stretch to rupture  $\lambda_R$ ; solid line is a Weibull distribution fitted to the data.

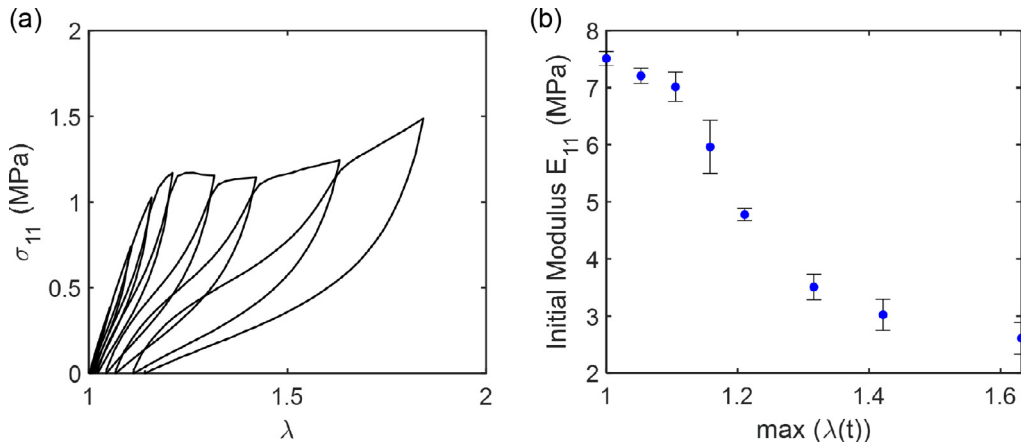


**Fig. 4.** (a) The stress-stretch response of a longitudinal specimen with 3 vol.% glass fibers upon subsection to cyclic loading to increasing stretch, comparable to the Mullins effect; (b) Initial modulus vs. maximum stretch for each loading cycle.

local stretch field for both longitudinal and transverse loading during uniaxial tension, corresponding to the stretch values indicated by the red marks in Fig. 6b. For specimens loaded longitudinally (parallel with the fiber direction), deformation is approximately homogeneous for small deformation ( $\lambda_1$  to  $\lambda_2$ ). Non-homogeneous deformation becomes evident for  $\lambda \geq \lambda_2$ , where the stress-stretch data indicates the onset of softening. Following initial yielding ( $\lambda = \lambda_3$ ), the region of high stretch grows but remains somewhat localized as a band. Within this region the maximum local stretch is approximately 3, while the globally-applied stretch is only 1.43. As the sample is subject to further loading, the region of high stretch grows and eventually takes up the entire field of view. In contrast, the specimens loaded transversely (perpendicular to the fiber direction) exhibit much more homogeneous stretch fields at all values of applied stretch. As another way to capture these

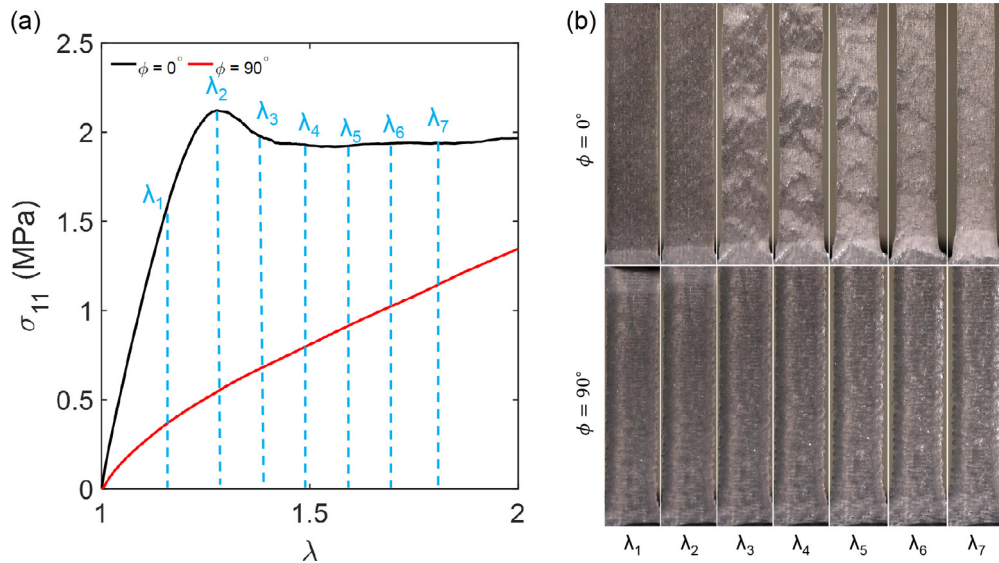


**Fig. 5.** (a) Experimental stress-stretch behavior of longitudinal (black) and transverse (red) samples with 5 vol.% glass fibers; (b) optical images of the samples when stretched to the indicated stretch level. (For interpretation of the references to colour in this figure legend, the reader is referred to the web version of this article.)

different deformation patterns, Fig. 6(c) shows the standard deviation  $s(\lambda)$  of the stretch within the field of view as a function of the applied stretch. For longitudinal loading,  $s(\lambda)$  increases significantly between  $\lambda_2$  and  $\lambda_3$ , coinciding with the appearance of localized stretching in Fig. 6(a). This quantity continues to rise until  $\lambda_5$ , at which point the total regions of elevated local stretch account for nearly half the sample. On the other hand,  $s(\lambda)$  remains very low for transverse loading, in agreement with the observed homogeneous stretch field.

### 3.3. In situ microstructural characterization

To understand the origin of the non-homogeneous deformation and stress-stretch behavior we characterize the evolution of the microstructure during loading. Tensile specimens were stretched under a microscope to allow high-resolution *in situ* optical measurements. These images were used to both observe the evolution of the local microstructure (e.g., fiber realignment and matrix-fiber debonding) and to perform microscale DIC, giving high-resolution stretch fields. The full field stretch maps are shown in Fig. 7(a) for the four loading steps ( $\lambda_1$ ,  $\lambda_3$ ,  $\lambda_5$ ,  $\lambda_7$ ) indicated in Fig. 7(b). These indicate that the non-uniform stretch field observed at the macroscale is also a feature at the microscale. The standard deviation of the field  $s(\lambda)$  is again plotted in Fig. 7(c). The composites loaded longitudinally show significant non-homogeneous deformation, whereas the samples loaded transversely do not.

Local damage can be observed in the microscope images during stretch. Fig. 8(a) shows the reference image for a longitudinally-loaded sample before stretching with overlay of the stretch map for  $\lambda = \lambda_7$  in Fig. 7(b). We chose to monitor two regions closely during stretching, indicated by the yellow and blue boxes in Fig. 8(a). The yellow region has a high degree of deformation and the blue region has relatively low deformation. Enlarged images of these two regions are shown for four different values of applied stretch in Fig. 8(b). Within the high-stretch (yellow) region, fiber debonding can be seen as early as the first loading step ( $\lambda \approx 1.035$ ). By the third loading step ( $\lambda \approx 1.105$ ), a large number of fibers in this region have debonded from the matrix. By the fifth loading step ( $\lambda \approx 1.14$ ), almost all fibers within the region have partially or fully debonded from the matrix. In contrast, the small-stretch (blue) region only shows a small amount of fiber debonding across all loading steps. The co-location of the fiber debonding in the regions of high local deformation and whitening indicates that the fiber debonding is the underlying mechanism producing the softening in the stress-stretch curves, the localization of stretch during deformation, and the macroscopic whitening.

## 4. Modeling

### 4.1. Micromechanical model

To better understand the experimental data and the importance of the observed fiber-matrix debonding we developed a micromechanical model derived from a simple extension of the shear lag model (Cox, 1952; Ghassemieh and Nassehi, 2001; Hull and Clyne, 1996). We incorporated the experimentally-measured fiber length distribution and fiber-matrix debonding probability by adding a Weibull distribution to the shear lag model. In the shear lag model, fibers and matrix are assumed

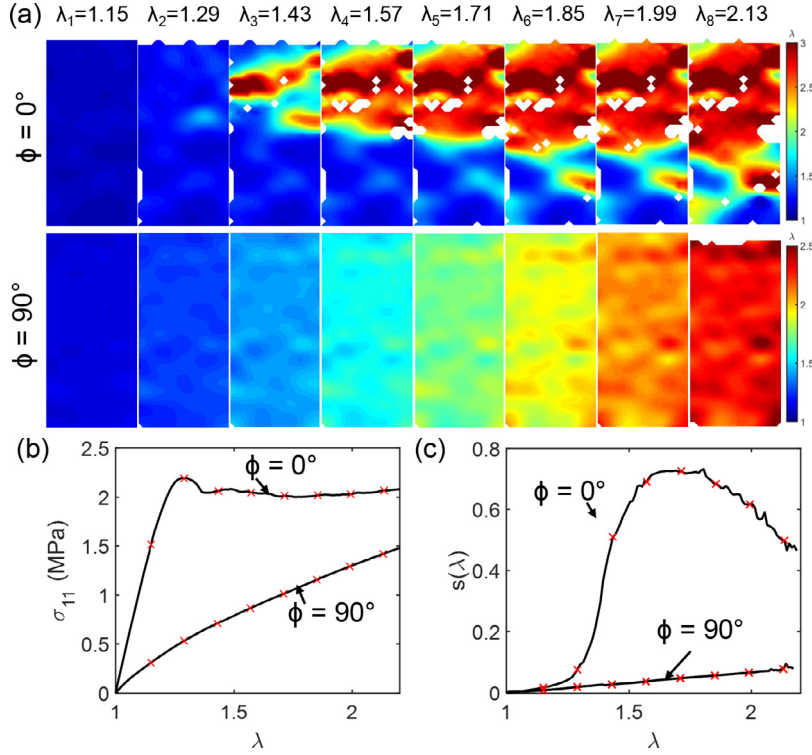


**Fig. 6.** Non-homogeneous deformation observed at the macroscale: (a) Full-field stretch maps recorded via DIC at the stretch values indicated in panels (b) and (c), for both longitudinal ( $\phi = 0^\circ$ ) and transverse ( $\phi = 90^\circ$ ) loading; (b) representative experimental stress-stretch curves for both samples; (c) standard deviation of the local stretch values measured across the full sample as a function of the globally-applied stretch.

to be initially perfectly bonded. With the application of an external load, the applied stress is transferred from matrix to fibers by means of interfacial shear stress at the fiber-matrix interface and normal stretching at the ends of fibers. The stress-stretch relationship (Ghassemieh and Nassehi, 2001; Hull and Clyne, 1996) for this ideal case is

$$\sigma = (\lambda - 1) \left[ f E_f \left( 1 - \frac{(E_f - E') \tanh(ns_0)}{E_f ns_0} \right) + (1 - f) E_m \right] \quad (1)$$

with

$$n = \left[ \frac{2E_m}{E_f(1 - \nu_m) \ln(1/f)} \right]^{1/2} \quad (2)$$

and

$$E' = \frac{E_f[1 - \text{sech}(ns_0)] + E_m}{2} \quad (3)$$

where  $f$  is the volume fraction of fibers,  $E_f$  and  $E_m$  are the stiffness of fiber and matrix, respectively,  $\nu_m$  is the Poisson's ratio of the matrix, and  $s_0 = L/r$  is the ratio of half length  $L$  and radius  $r$  of the fiber. With increasing external loading the shear at the fiber-matrix interface increasingly distorts the matrix, producing a maximum shear stress at the ends of the fibers. The maximum interfacial shear stress is:

$$\tau_i = \frac{n(\lambda - 1)}{2 \coth(ns_0)} E_f \quad (4)$$

Once debonding of the fiber and matrix initiates, the length of the bonded region,  $L_t$ , decreases, producing a stress transfer aspect ratio  $s_t = L_t/r$  that is calculated by taking  $\tau_i = \tau_c$  in Eq. (4), where  $\tau_c$  is the critical shear stress for the fiber-matrix interface:

$$s_t = \frac{1}{n} \coth^{-1} \left( \frac{n(\lambda - 1)}{2\tau_c} E_f \right) \quad (5)$$

A Weibull distribution is introduced in the model to indicate the probability of debonding,  $P_f$ , at the fiber-matrix interface for a given fiber length  $L$  and shear stress  $\tau_i$ :

$$P_f = 1 - \exp \left[ - \frac{L}{L_c} \left( \frac{\tau_i}{\tau_c} \right)^m \right] \quad (6)$$

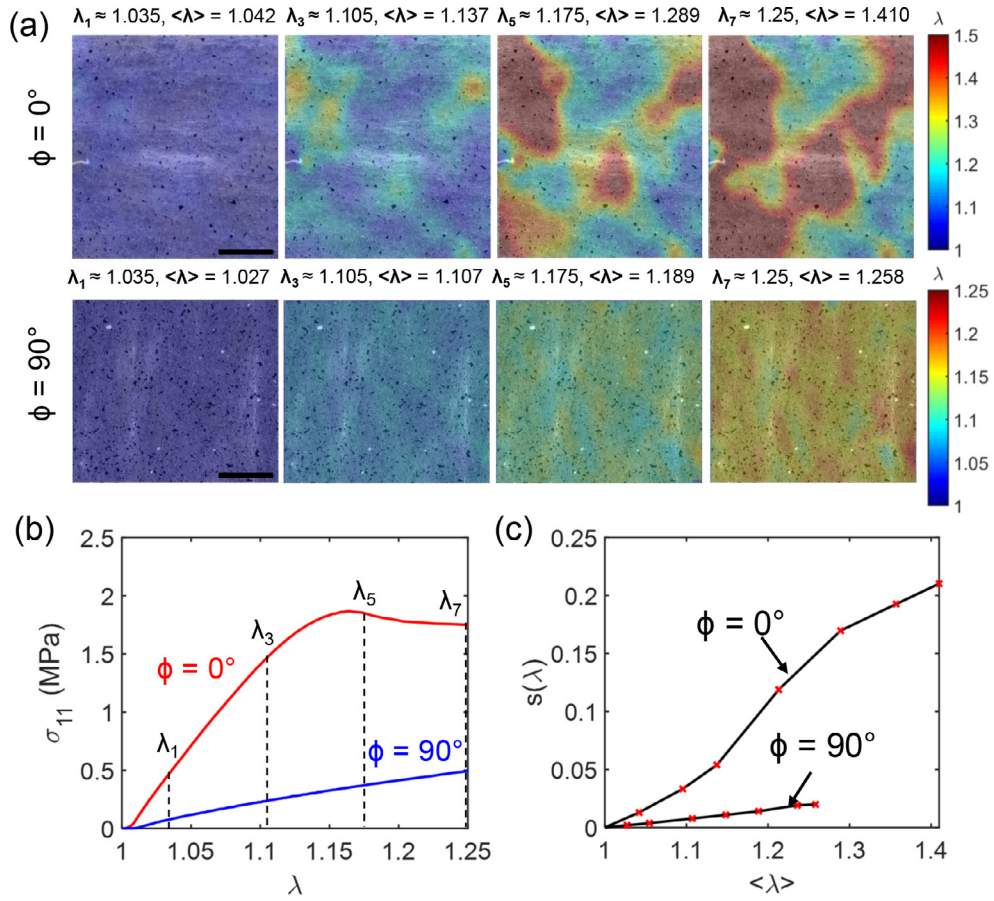


**Fig. 7.** Non-homogeneous deformation observed at the microscale: (a) Full-field stretch maps recorded via DIC at the approximate stretch values indicated in panel (b); scale bars are  $500\mu\text{m}$ ; (b) representative stress-stretch plots for both samples; (c) standard deviation of the local stretch values measured across the full sample.

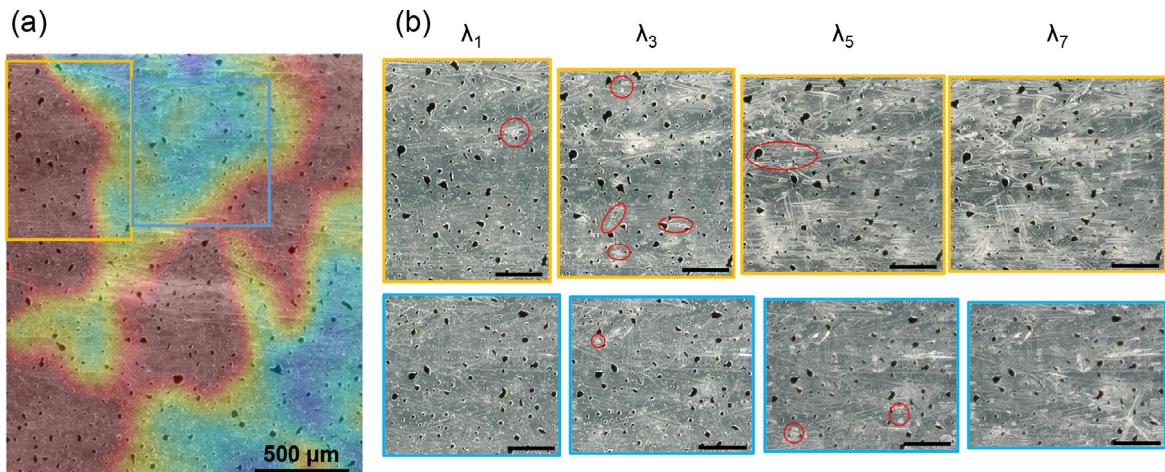


**Fig. 8.** Fiber-matrix debonding during deformation: (a) micrograph of an undeformed specimen with the final local stretch map overlaid (from Fig. 7a); (b) micrographs of the yellow and blue regions indicated in panel a, here with global stretch applied (all scale bars are  $200\mu\text{m}$ ); red markers indicate newly-debonded fibers. (For interpretation of the references to colour in this figure legend, the reader is referred to the web version of this article.)

where  $L_c$  is a length of fiber associated with the shear stress at  $\tau_c$ , and  $m$  is the Weibull modulus. The probability that the fibers remain fully bonded to the matrix is then  $P_s = 1 - P_f$ . From Eqs. (1) and (6), the stress-stretch relationship becomes

$$\sigma = (\lambda - 1) \left[ f P_s E_f \left( 1 - \frac{(E_f - E') \tanh(ns_0)}{E_f n s_0} \right) + f P_f E_f \left( 1 - \frac{\tanh(ns_t)}{n s_t} \right) + (1 - f) E_m \right] \quad (7)$$

The fiber length distribution in the printed samples is measured as described in Section 2.1, giving a mean and standard deviation for  $P_L$ , which is incorporated into the modified shear lag model as:

$$\sigma = (\lambda - 1) \left[ f E_f \int_0^\infty \left[ P_s \left[ 1 - \frac{(E_f - E') \tanh(ns_0)}{E_f n s_0} \right] + P_f \left[ 1 - \frac{\tanh(ns_t)}{n s_t} \right] \right] P_L dL + (1 - f) E_m \right] \quad (8)$$

#### 4.2. Constitutive model

The micromechanical model proposed above is useful for providing mechanistic insight into the failure process of our material. However, it is often difficult to apply in complex loading scenarios. As a more practical tool, we developed a constitutive model for these fiber-reinforced composites that makes use of a damage parameter. For a fiber-reinforced incompressible non-linear elastic solid, the constitutive response can be modeled using the strain energy function as follows (Merodio and Ogden, 2005a):

$$W = W_m(I_1, I_2, I_3) + W_f(I_4, I_5) \quad (9)$$

where  $I_1$  to  $I_3$  are the invariants of the right Cauchy-Green Deformation tensor  $\mathbf{C} = \mathbf{F}^T \mathbf{F}$  with deformation gradient  $\mathbf{F} = \partial \mathbf{x} / \partial \mathbf{X}$ , and  $\mathbf{X}$  and  $\mathbf{x}$  are the position vectors in the reference and the deformed configurations, respectively.  $I_1$  to  $I_3$  are defined as:

$$I_1 = \text{tr } \mathbf{C}, \quad I_2 = \frac{1}{2} [(\text{tr } \mathbf{C})^2 - \text{tr}(\mathbf{C}^2)], \quad I_3 = \det \mathbf{C} \quad (10)$$

$I_4$  and  $I_5$  are additional invariants with fiber reinforcement in a direction defined by a unit vector  $\mathbf{A}$ :

$$I_4 = \mathbf{A} \cdot (\mathbf{C} \mathbf{A}), \quad I_5 = \mathbf{A} \cdot (\mathbf{C}^2 \mathbf{A}) \quad (11)$$

Damage is incorporated in both the matrix and fiber strain energy terms following the pseudo-elastic model introduced by Ogden and Roxburgh (Ogden and Roxburgh, 1999). The scalar  $d_m$  represents the damage from the virgin state of the matrix material, which is history dependent, and  $d_f$  represents damage to the fiber reinforcement:

$$W = (1 - d_m) W_m + \phi_m(d_m) + (1 - d_f) W_f + \phi_f(d_f) \quad (12)$$

The damage function is defined such that  $\phi(0) = 0$ , and the Cauchy stress takes the form:

$$\mathbf{T} = (1 - d_m) \overline{\mathbf{T}}_m + (1 - d_f) \overline{\mathbf{T}}_f \quad (13)$$

$\overline{\mathbf{T}}_m$  and  $\overline{\mathbf{T}}_f$  are the Cauchy stress resulting from undamaged strain energy. Both damage parameters are related, as shown in the previous section, by sharing the same underlying mechanism of fiber debonding. Debonding contributes to the matrix damage term due to void nucleation at the debonding sites. Debonding contributes to the fiber damage term as less stress is transferred from the matrix to the fibers. Since both terms depend on the same mechanism, we expect the two damage parameters to take the same form, defined in previous work (Guo and Sluys, 2006; Li, 2016):

$$d_i(\alpha_i) = 1 - \exp\left(-\frac{\alpha_i}{\beta}\right) \quad (14)$$

where  $i$  can be either  $m$  or  $f$ , corresponding to matrix and fiber, respectively.  $\beta$  is a model parameter which determines the rate of damage. Eq. (14) suggests the damage is related exponentially to some effective strain energy function, referred to as the damage evolution parameter  $\alpha_i(\lambda)$  under uniaxial loading with stretch  $\lambda$  (Marini et al., 2012; Peña, 2011):

$$\alpha_i(\lambda) = \max\left(\sqrt{2W_i(\lambda)} - \sqrt{2W_i(\lambda_c)}, 0\right) \quad (15)$$

Where  $\lambda_c$  is the stretch at which damage would start to occur. This definition implies  $\alpha$  (same as  $d_i$ ) will remain zero before deformation reaches  $\lambda_c$ . Note the damage evolution for both matrix and fiber reinforcement is controlled by a sole shared fitting parameter  $\beta$  reflecting the mechanistic relationship between matrix and fiber damage.

The matrix damage  $d_m$  is primarily responsible for modeling loading and unloading behavior of the matrix material, which takes the form (Ogden and Roxburgh, 1999):

$$d_m = \begin{cases} 0, & \text{if } \alpha_m \text{ is reached for the first time.} \\ d_m \left( \max_{s \in [-\infty, t]} \alpha_m(\lambda(s)) - \alpha_m \right), & \text{otherwise.} \end{cases} \quad (16)$$

**Table 1**

Parameters used to fit the micromechanical model to experiments.

	$L_c$ ( $\mu\text{m}$ )	$L_0$ ( $\mu\text{m}$ )
3%	50	$110 \pm 42$
5%	70	$108 \pm 39$
10%	130	$75 \pm 37$

However the fiber reinforcement damage  $d_f$  is primarily responsible for modeling the softening of the primary loading curve. Hence we use the form of damage defined by Simo (Simo, 1987):

$$d_f = \begin{cases} d_f(\alpha_f) & , \text{ if } \alpha_f \text{ is reached for the first time.} \\ d_f\left(\max_{s \in [-\infty, t]} \alpha_f(\lambda(s))\right) & , \text{ otherwise.} \end{cases} \quad (17)$$

Both damage for matrix and fibers depend on the loading history per the definitions. First, during monotonic loading the matrix damage will not initiate ( $d_m = 0$ ). Secondly, the fiber damage will not decrease during loading and unloading.

We use the Holzapfel-Gasser-Ogden (HGO) model (Holzapfel et al., 2000) to capture the response of our fiber-reinforced hyperelastic material with an incompressible matrix, as in our previous work that used similar material (Jiang et al., 2019):

$$W_m = \frac{\mu}{2}(I_1 - 3)$$

$$W_f = \frac{\mu k_1}{2k_2} [e^{k_2(I_4 - 1)^2} - 1] \quad (18)$$

For this proposed strain energy function, the corresponding Cauchy stress for each virgin strain energy under uniaxial stretch can be expressed as (Bower, 2009; Merodio and Ogden, 2005a; Ogden and Roxburgh, 1999):

$$\bar{T}_m = \mu \left( \lambda^2 - \frac{1}{\lambda} \right)$$

$$\bar{T}_f = 2\mu k_1 (I_4^2 - I_4) e^{k_2(I_4 - 1)^2} \quad (19)$$

The invariant  $I_4$  can be directly expressed from the stretch  $\lambda$  and fiber orientation  $\phi$  when the material is under uniaxial stretch:

$$I_4 = \lambda^2 \cos^2 \phi + \lambda^{-1} \sin^2 \phi \quad (20)$$

In the case of loading along the fiber direction ( $\phi = 0^\circ$ ),  $I_4 = \lambda^2$ . The Cauchy stress in the stretch direction can be computed as:

$$\mathbf{T}_{11} = (1 - d_m) \bar{T}_m + (1 - d_f) \bar{T}_f \quad (21)$$

The stress consists of contributions from the matrix  $T_m$  and from the fiber  $T_f$ , with the latter being related to the stress damage parameter. Five parameters are required for the constitutive model presented here: material-related constants  $\mu$ ,  $k_1$ , and  $k_2$ , and damage-related constants  $\beta$  and  $\lambda_c$ . Finally, to fit our experimental results the Cauchy stress can be transformed to nominal stress as follows:

$$\sigma_{11} = \lambda^{-1} \mathbf{T}_{11} \quad (22)$$

## 5. Discussion

### 5.1. Micromechanical model results

To start, the micromechanical model Eq. (8) is calibrated as a function of volume fraction using the experimental stress-stretch curves obtained from longitudinal specimens. Fig. 9(a) shows the results of this fit, with parameters  $E_f=60$  GPa,  $\nu_m=0.45$ ,  $r=15\mu\text{m}$ ,  $E_m=2.2$  MPa,  $\tau_c=4$  MPa, and Weibull parameter  $m=5$ . Our modified shear lag model captures the features of all three cases, with only variations in the fiber length distribution, which is experimentally measured for each volume fraction, and the critical length  $L_c$  (Table 1). These fiber length distributions are shown in Fig. 9(b). The length distributions do not vary significantly at lower volume fractions (3% and 5%). However, as the fiber volume fraction increases, the average fiber length suddenly decreases, before again plateauing for higher volume fractions (8% and 10%). Interestingly, this again fits the pattern of a Weibull distribution. By incorporating the Weibull fit in our micromechanical model properties that will vary with volume fraction but which were not experimentally measured can be predicted. For example, Fig. 9(c) shows the debonding probability Eq. (6) for various volume fractions using the Weibull fitting parameters. Each plot also indicates the stretch to rupture  $\lambda_R$  for each volume fraction and the fiber length distribution, both obtained empirically. (Note the fiber

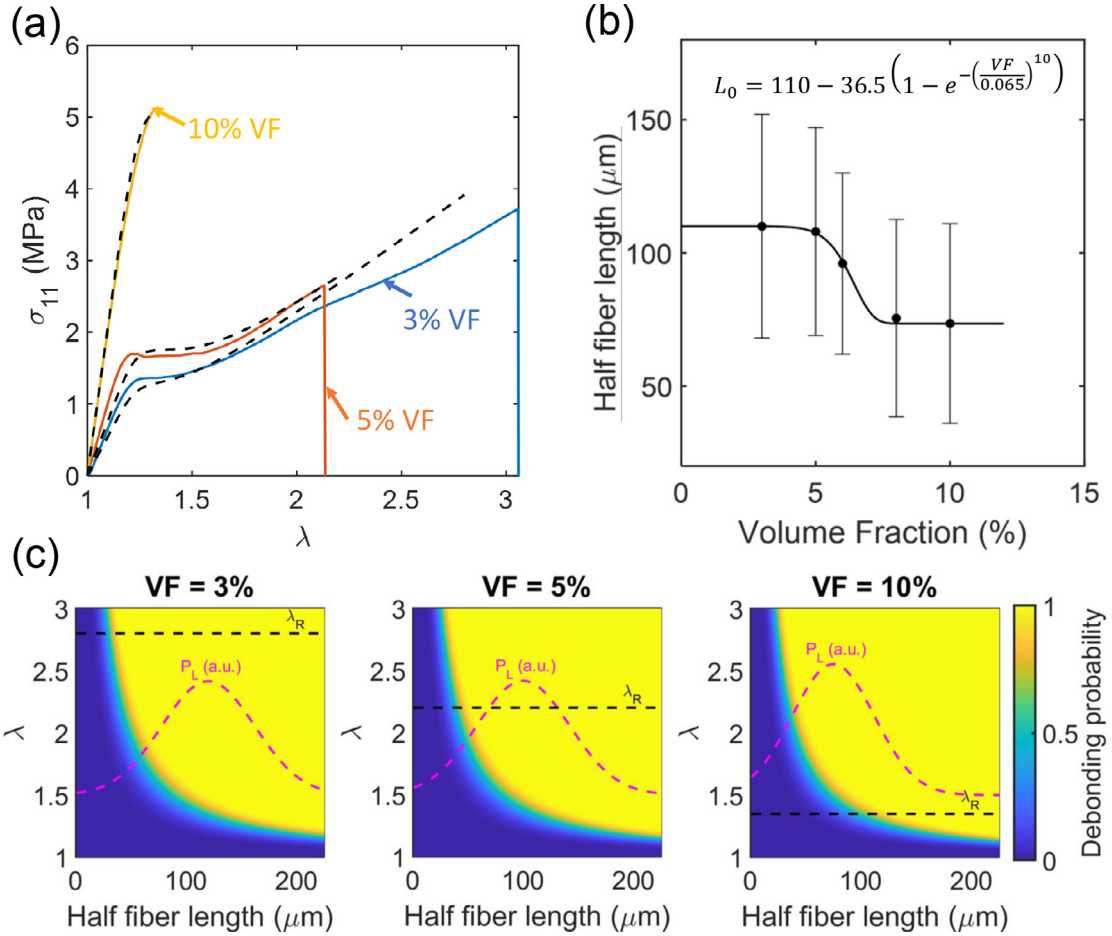


**Fig. 9.** (a) Fitting using the micromechanical model; (b) Fiber length distribution as a function of volume fraction, measured experimentally; (c) probability of fiber debonding for three volume fractions, with  $\lambda_R$  and unscaled fiber length probability  $P_L$  overlaid.

length distribution is not scaled in the plot.) This schematic helps explain how to compute the contribution from the fibers in Eq. (8) by taking the fiber length distribution into account.

In addition to the fiber length distribution, the other parameter in the micromechanical model that was varied with volume fraction is the critical length  $L_c$ .  $L_c$  determines when damage initiates for fibers of various lengths. As  $L_c$  increases, the probability of debonding of a fiber increases at a set fiber length and stretch value. As a result, the debonding probability plot shown in Fig. 9(c) will shift down. Physically, a larger  $L_c$  will result in earlier onset of debonding. We vary the value of  $L_c$  and calculate the mechanical properties such as initial modulus  $E_{11}$  and strength  $S_{11}$  using the computed stress-stretch curve from the micromechanical model for each volume fraction. The ultimate tensile stress is calculated as  $\sigma_{11}(\lambda_R)$ , where  $\lambda_R$  for each volume fraction is calculated using the empirical fit Weibull distribution for stretch to rupture shown in Fig. 3(d). The result is shown in Fig. 10(a) and (b). This shows that by increasing  $L_c$  the initial modulus and strength at a given volume fraction will generally increase, except for the evident decrease in strength at lower volume fractions. This latter effect is a result of the much higher rupture stretches  $\lambda_R$  at lower volume fraction (hence the ultimate tensile stress is essentially that of matrix). Additionally, the initial modulus  $E_{11}$  does not show perfectly linearly monotonic behavior. There is a slight plateau around the transition volume fraction (6 vol.%), the point at which the fiber lengths start to decrease. Similarly, the ultimate strength also reverses its trend at this volume fraction as it increases with increasing fiber volume fraction.

Another parameter from the micromechanical model is  $\tau_c$ , the interfacial shear strength between matrix and fibers, which is a physical quantity that could in principle be tuned by adjusting adhesion strength between the matrix and fiber. However, since the materials and fabrication approach do not vary from sample to sample,  $\tau_c$  remains unchanged. Hypothetically, there are a variety of ways to change this property. For example, plasma treatment can be used to improve the adhesion strength between PDMS and glass fibers. The effect of  $\tau_c$  on the mechanical properties is also computed and shown in Fig. 10(c) and (d). Similar to the trends for  $L_c$ , an increase in  $\tau_c$  generally increases both the initial modulus and strength for a given volume fraction. Interestingly, an increase in  $\tau_c$  initially increases the initial modulus significantly, though it has a minimal effect at higher values. Fig. 10(e) and (f) show the fit from the micromechanical model together

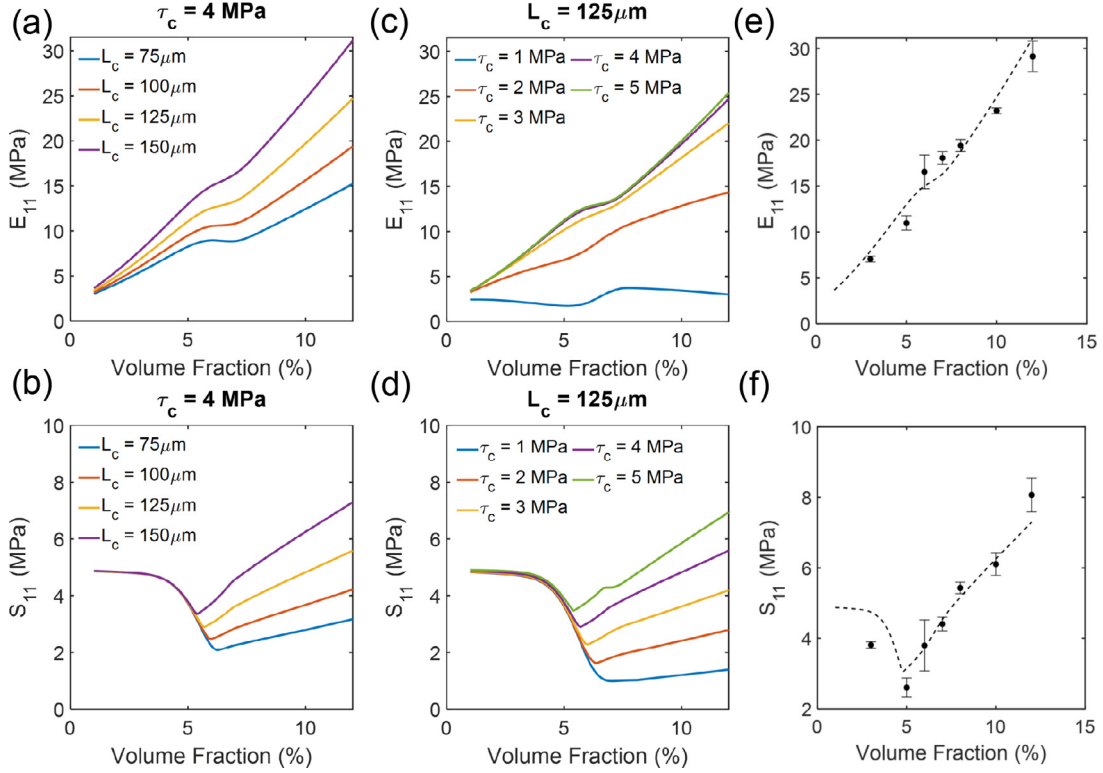


**Fig. 10.** Effect of (a-b)  $L_c$  and (c-d)  $\tau_c$  on mechanical properties. (e) Initial modulus  $E_{11}$  and (f) ultimate tensile strength  $S_{11}$  for various volume fractions using values of  $\tau_c = 4$  MPa and  $L_c = 150\mu\text{m}$  as model parameters, fitted by experiments.

**Table 2**  
Parameters used to fit the constitutive model to experiments.

	$\mu$ (MPa)	$k_1$	$\beta$	$\lambda_c$
3%	1.23	0.55	0.25	1.17
5%	1.5	0.9	0.30	1.17
10%	1.5	2.4	1.0	1.17

with the experimental results previously shown in Fig. 3(b) and (c). The model correctly predicts the non-monotonic trend in strength as a function of volume fraction, with an initial decrease followed by a large increase. The model also predicts the kink in the initial modulus ( $E_{11}$ ) versus volume fraction.

The micromechanical model provides insights to the change in mechanical properties as a function of fitting parameters that have physical significance, such as the fiber length distribution and the interfacial shear strength between matrix and fibers. The simple model predicts even the subtle anomalous effects observed in the experiments for the mechanical behavior as a function of volume fraction.

## 5.2. Constitutive model results

The experimental stress-stretch curves (solid) and their corresponding fit using the constitutive model (dashed) are shown in Fig. 11(a), showing good agreement across the relevant range of volume fractions. The values of the constitutive model's parameters used to fit the model to experiments are shown in Table 2. These parameters include material parameters  $\mu$ ,  $k_1$ , and  $k_2$ , and damage evolution parameters  $\beta$  and  $\lambda_c$ . The material parameter  $\mu$  corresponds to the matrix material while  $k_1$  is the fiber reinforcement factor.  $k_1$  is a function of the fiber volume fraction, with larger volume fractions leading to larger values of  $k_1$ . The effect of  $k_2$  is insignificant, similar to previous results (Jiang et al., 2019). The damage evolution is controlled by  $\beta$ , with larger  $\beta$  indicating slower damage evolution. In addition, the constitutive model can accurately predict the effect of fiber orientation. Using the definition of the invariant from Eq. (20), we fit the experimental results for 5 vol.% fibers with various orientations as shown in Fig. 11(b). To fit the model to loading scenarios with different orientations we fixed the material parameters, only allowing damage evolution parameters  $\beta$ , and  $\lambda_c$  to vary. These plots

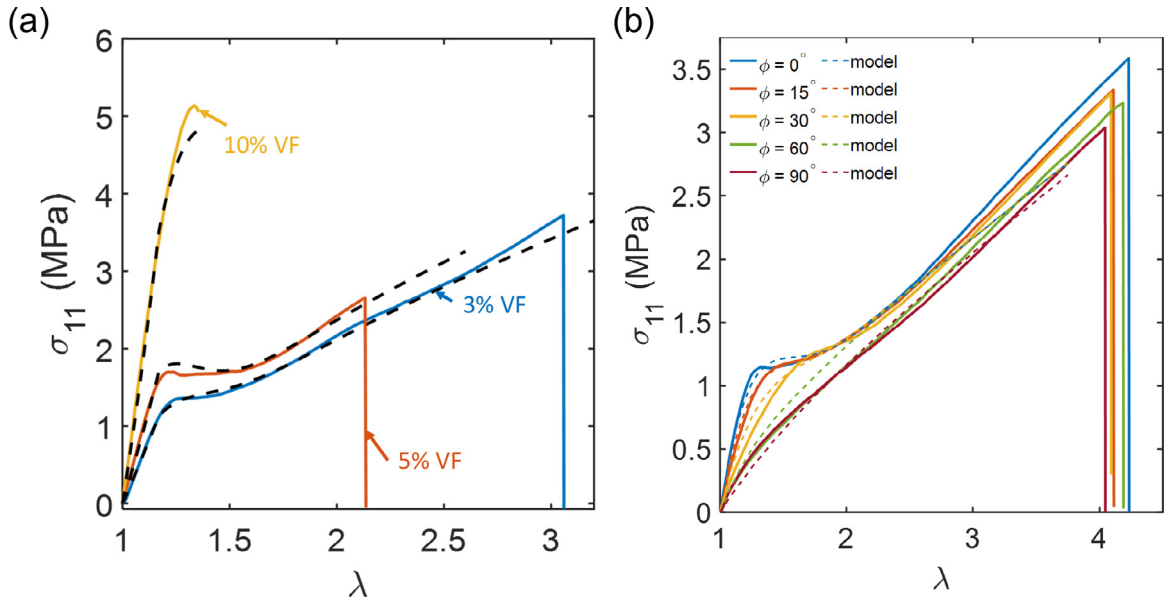


**Fig. 11.** Fitting the constitutive model (dashed) to experiments (solid) to capture the effect of (a) volume fractions and (b) fiber orientation on the stress-stretch behavior.

show that the constitutive model qualitatively captures the transition between softening behavior (observed when loading is mostly in the direction of the fibers) and matrix-dominated deformation (when loading perpendicular to the fibers).

The effect of damage evolution parameters on damage evolution is closely examined in Fig. 12. Since  $d_m$  is always 0 when the material is under monotonic loading, we only focus on  $d_f$  in analyzing monotonic fitting of the constitutive model. The evolution of damage  $d_f$  with various  $\beta$  during longitudinal loading is plotted in Fig. 12(a). The damage initiates when the stretch approaches the critical stretch  $\lambda_c$  where  $\alpha(\lambda_c) = \alpha_0$ . As the damage shape parameter  $\beta$  increases the damage evolves slower.

Additionally, the fiber orientation can have a large influence on the damage evolution. The Cauchy stress due to fiber reinforcement and  $d_f$  are plotted for various fiber orientations in Fig. 12(b)–(d). Importantly, the fiber reinforcement when  $\phi = 90^\circ$  is negative throughout. This is consistent with the finding of instability and loss of ellipticity under such loading conditions (Budiansky and Fleck, 1993; Merodio and Ogden, 2005a; Moran and Shih, 1998; Triantafyllidis and Abeyaratne, 1983). The orientation also has a large effect on the shape of the damage parameters. The damage evolves more slowly as the loading becomes more perpendicular to the fiber alignment, as shown in Fig. 12(c). For smaller angles, the evolution of damage  $d_f$  follows similar behavior. The less aligned that the loading is with the direction of fiber alignment, the more slowly the damage evolves, even with the same damage evolution parameter. However, for this more perpendicular loading the stress increase due to reinforcement is already much lower at larger stretch values, as shown in Fig. 12(b). The stress contributed from the fiber reinforcement to the damage model is shown in Fig. 12(d), showing the ability of the continuum model to capture the softening observed in experiments. The ability of the continuum model to capture damage evolution and many details of the stress-stretch response under various loading configurations makes it a potentially useful approach in modeling the mechanical response of fibrous composites with more complex, heterogeneous distributions of fiber alignment, as is possible with 3D printing (Jiang et al., 2019; Jiang and Raney, 2019; Raney et al., 2018). However, the implementation of the model under complex loading conditions should be performed carefully. As pointed out in the experimental results, deformation of the PDMS-GF composite material can be highly heterogeneous. A large enough domain should be considered such that these heterogeneities are averaged out to ensure an accurate overall response of the material.

The other advantage of the constitutive model is its handling of the damage state of the composite as a function of loading history. This can be used to model the Mullins-like effect that was observed in cyclic-loading experiments (Fig. 4). The fitting using this damage model for loading and unloading is shown in Fig. 13. The stress-stretch response with loading history identical to the experiments is shown in Fig. 13(a). During initial loading, the material exhibits an elastic response with no hysteresis, as no damage is initiated when  $\lambda < \lambda_c$ . As loading crosses the critical stretch  $\lambda_c$  where softening occurs during uniaxial loading, damage develops and a hysteresis is observed during loading and unloading. The loading and unloading dependence is incorporated in both damage parameters,  $d_m$  and  $d_f$ , which share a common fitting parameter  $\beta$ , as described in the previous section. As discussed for the case of monotonic loading,  $\beta$  represents the rate of damage evolution. The experimental result of the Mullins-like behavior is also revealed in changes in the initial modulus with increasing deformation. Under the pseudo-elastic constitutive model, one can extract the fiber damage evolution from the degradation

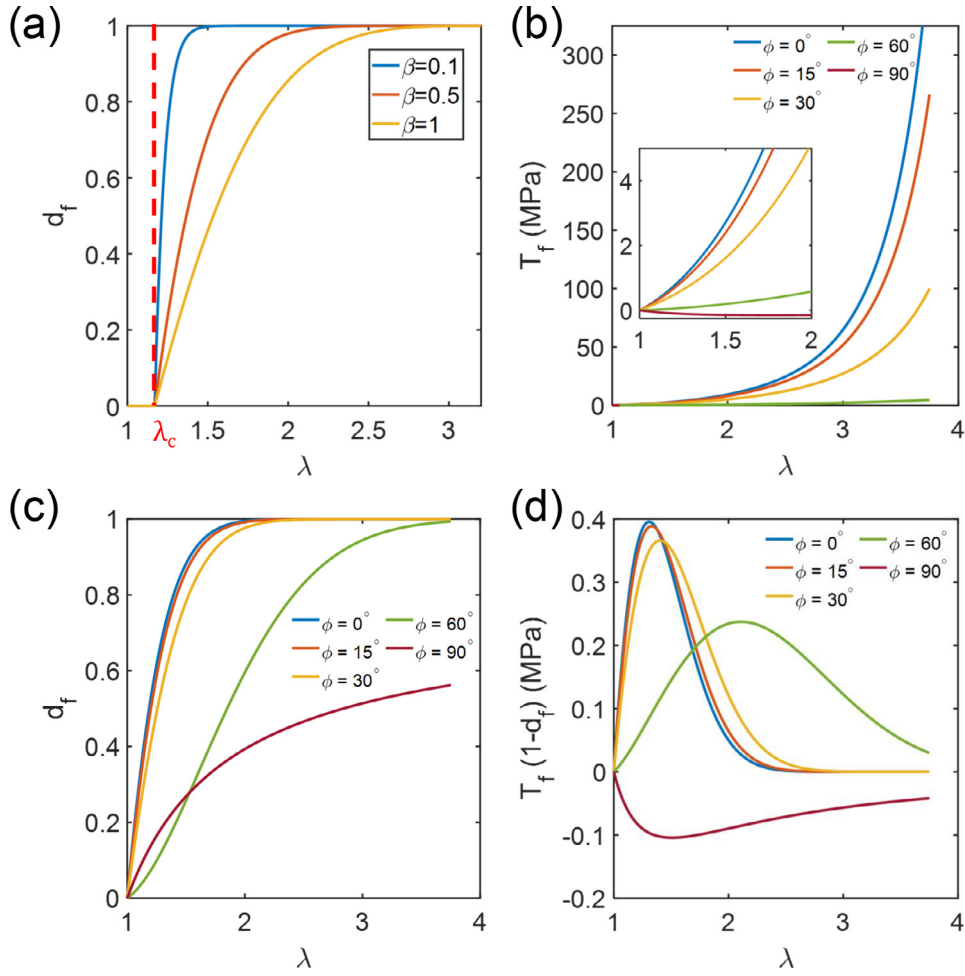


**Fig. 12.** (a) Effect of the damage evolution parameters for  $\phi = 0^\circ$ . Effect of the fiber orientation on, respectively, (b) the Cauchy stress from fiber reinforcement  $T_f$  (inset shows this at lower stretch values), (c) damage evolution for  $\beta = 0.35$  and  $\lambda_c = 1$ , and (d) damaged Cauchy stress from fiber reinforcement.

of the initial modulus as (Diani et al., 2009; Ogden and Roxburgh, 1999):

$$\frac{E(\lambda_1) - E_{\min}}{E(\lambda_2) - E_{\min}} = \frac{1 - d_f(\lambda_1)}{1 - d_f(\lambda_2)} \quad (23)$$

where  $E_{\min}$  is the stiffness of the fully-damaged material. With this condition, initial stiffness during reloading can be expressed as a function of the maximum stretch achieved previously:

$$E(\lambda) = E_{\min} + (1 - d_f)(E_{\max} - E_{\min}) \quad (24)$$

where  $E_{\max}$  is the stiffness of the undamaged composite material, which can be extracted from the experimental results. Using Eq. (17), the damage parameter  $d_f$  can be fit to the experiments, as shown in Fig. 13 b. The fiber damage evolution parameter produces the exponential degradation in initial modulus, as observed in experiments.

The damage evolution is shown in Fig. 13(c) and (d) for  $d_m$  and  $d_f$ , respectively. The unloading path is largely a function of the maximum effective strain energy, as described in Eq. (16). The damage to fiber reinforcement  $d_f$  is seen to hold during unloading and reloading until it exceeds the prior maximum. The loading portion maps out the damage per monotonic loading shown in Fig. 12(a). Most interestingly, the best fit of  $d_f$  using the experimental data in Fig. 13(b) is also plotted here as a dashed line, which is very close to the model parameter used to fit the Mullins-like result. However, there are still a few key differences between the experimental results and our model. First, our experiments show separate loading and unloading behavior with hysteresis which is not the case in the model. Secondly, our model does not account for residual stretch after unloading, unlike observations in experiment. Both of these differences could be addressed by adding parameters that control the residual stretch as a function of maximum strain energy as suggested in previous literature (Dorfmann and Ogden, 2004). However, these phenomena are not the focus of the present work, and we therefore focus here on the use of our

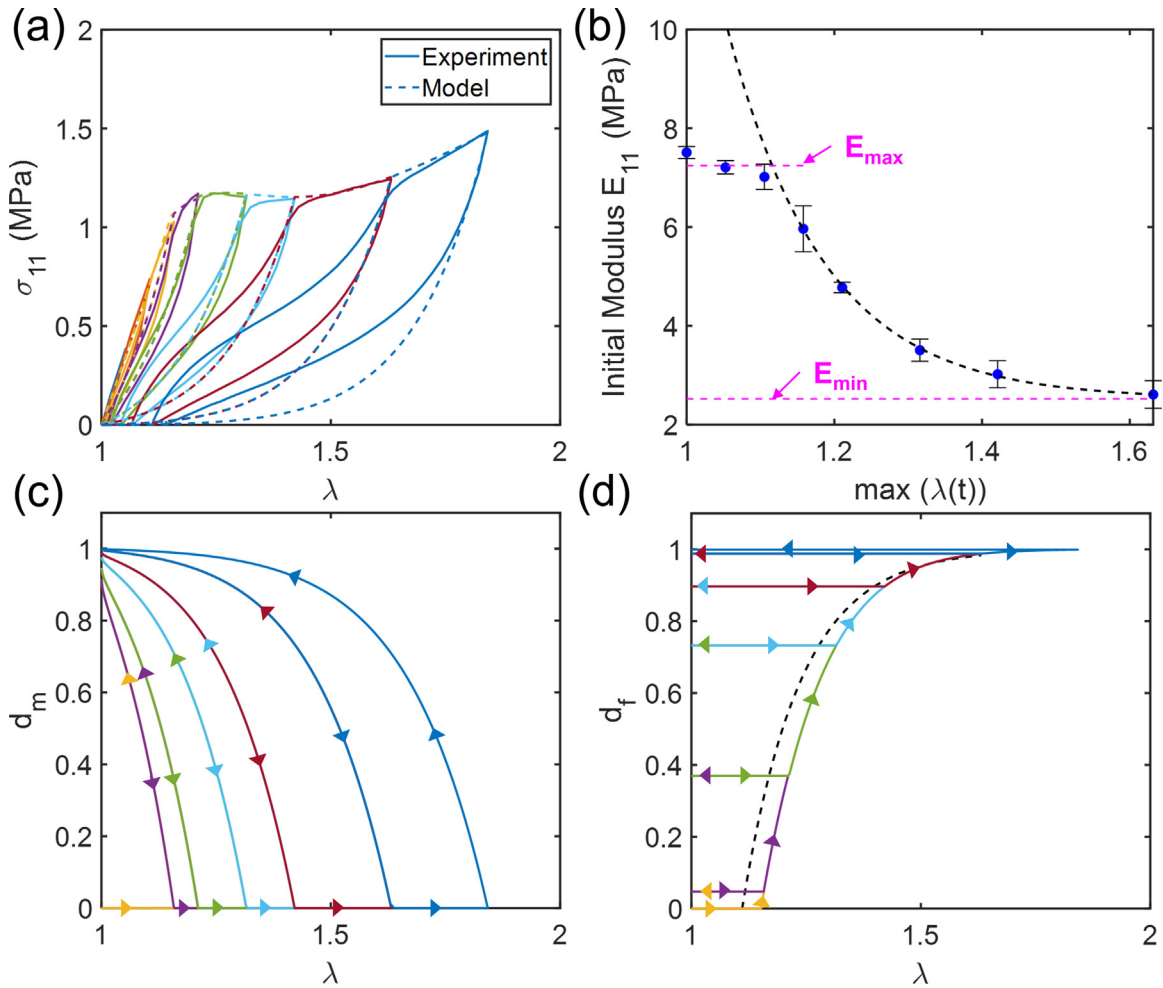


**Fig. 13.** (a) Plot showing fitting of the constitutive model to the cyclic experimental data exhibiting the Mullins-like effect; (b) Best fit to the experiments using the damage model in Eq. (17). The dashed curve is the best fit to the experimental data using Eq. (24). Damage evolution during loading and unloading for (c) matrix damage  $d_m$  and (d) fiber reinforcement damage  $d_f$ . The dashed curve in (d) is calculated from the best fit shown in (b), from Eq. (24).

phenomenological model that demonstrates the promise of accurately predicting the loading behavior and damage evolution in the 3D-printed composite with the fewest number of parameters.

## 6. Conclusion

In summary, we have fabricated short fiber composites with a soft, nearly incompressible matrix and controlled fiber orientation using 3D printing. We have performed a systematic study of the effects of volume fraction and fiber orientation on the mechanical response. Contrary to classical models, the ultimate tensile strength does not increase monotonically with volume fraction. Instead, a sharp transition is observed with increasing volume fraction from a regime with substantial softening and ductility at lower volume fractions to a regime with low rupture stretch and no softening at higher volume fractions, leading to a non-monotonic strength increase. We also observed history-dependent behavior comparable to the Mullins effect under reloading of the specimens. To better understand the mechanism causing the softening, we conducted *in situ* optical imaging and digital image correlation during loading experiments, at both macroscopic and microscopic length scales. This allowed us to identify fiber debonding as the cause of the mechanical softening, and to relate it to the observed whitening and non-homogeneous deformation, an effect most pronounced when loading is parallel with the fiber direction (longitudinal). These effects are not observed when loading is perpendicular to the direction of fiber alignment (transverse), which is explained by the anisotropy of the fibrous reinforcement. Furthermore, we developed two models to explain the macroscopic response for different volume fractions and fiber orientations: i) a micromechanical model and ii) a constitutive model. Both models provide direct insight into damage evolution in the composite, and accurately predict the mechanical behavior under various volume fractions and fiber orientations. The constitutive model is able to accurately fit the Mullins-

like response observed during cyclic loading in the experiments and to predict the damage parameter obtained via the degradation of modulus during these tests. The above fundamental understanding will enable future studies of failure in composites with more complex, spatially-varying fiber distributions that can now be produced via 3D printing.

### Declaration of Competing Interest

The authors declare that they have no known competing financial interests or personal relationships that could have appeared to influence the work reported in this paper.

### CRedit authorship contribution statement

**Chengyang Mo:** Conceptualization, Methodology, Investigation, Writing - original draft. **Yijie Jiang:** Conceptualization, Methodology, Investigation, Writing - original draft. **Jordan R. Raney:** Conceptualization, Methodology, Writing - review & editing.

### Acknowledgments

This research was partially supported by NSF through the University of Pennsylvania Materials Research Science and Engineering Center (MRSEC) (DMR-1720530) and by a 3M Non-Tenured Faculty Award. The authors thank Prof. Pedro Ponte Castañeda for helpful discussions about the work, Dr. Hangju Oh and Prof. Mark G. Allen for use of the optical microscope, and Dr. Jiasong Zhang and Prof. Kevin T. Turner for use of the tensile grips for *in situ* microscopic measurements.

### References

- Bechtle, S., Fett, T., Rizzi, G., Habelitz, S., Klocke, A., Schneider, G.A., 2010. Crack arrest within teeth at the dentin/enamel junction caused by elastic modulus mismatch. *Biomaterials* 31 (14), 4238–4247 doi:10.1016/j.biomaterials.2010.01.127. ISSN 01429612.
- Bircher, K., Zündel, M., Pensal, M., Ehret, A.E., Mazza, E., 2019. Tear resistance of soft collagenous tissues. *Nat. Commun.* 10, 792. doi:10.1038/s41467-019-08723-y.
- Blaber, J., Adair, B., Antoniou, A., 2015. Ncorr: Open-source 2d digital image correlation matlab software. *Exp. Mech.* 55 (6), 1105–1122 doi:10.1007/s11340-015-0009-1. ISSN 1741-2765.
- Blesgen, T., Fraternali, F., Raney, J.R., Daraio, C., 2013. Multiscale mass-spring models of carbon nanotube arrays accounting for mullins-like behavior and permanent deformation. *Multiscale Model. Simul.* 11 (2), 545–565.
- Boley, J.W., van Rees, W.M., Lissandrello, C., Horenstein, M.N., Truby, R.L., Kotikian, A., Lewis, J.A., Mahadevan, L., 2019. Shape-shifting structured lattices via multimaterial 4d printing. *Proceedings of the National Academy of Sciences of the United States of America* 116 (42), 20856–20862.
- Bower, A.F., 2009. *Applied Mechanics of Solids*, 1st CRS Press. ISBN 9781439802472.
- Budiansky, B., Fleck, N.A., 1993. Compressive failure of fibre composites. *Journal of the Mechanics and Physics of Solids* 41 (1), 183–211 doi:10.1016/0022-5096(93)90068-Q. ISSN 00225096.
- Compton, B.G., Lewis, J.A., 2014. 3D-printing of lightweight cellular composites. *Advanced Materials* 26 (34), 5930–5935. doi:10.1002/adma.201401804. ISSN 15214095.
- Cox, H.L., 1952. The elasticity and strength of paper and other fibrous materials. *B. J. Appl. Phys.* 3, 72–79.
- De Vita, R., Slaughter, W.S., 2007. A constitutive law for the failure behavior of medial collateral ligaments. *Biomechanics and Modeling in Mechanobiology* 6 (3), 189–197. doi:10.1007/s10237-006-0054-x. ISSN 1617-7959
- Diani, J., Fayolle, B., Gilormini, P., 2009. A review on the Mullins effect. *European Polymer Journal* 45 (3), 601–612. doi:10.1016/j.eurpolymj.2008.11.017. ISSN 0014-3057
- Dorfmann, A., Ogden, R.W., 2004. A constitutive model for the Mullins effect with permanent set in particle-reinforced rubber. *International Journal of Solids and Structures* 41 (7), 1855–1878. doi:10.1016/j.ijsolstr.2003.11.014. ISSN 00207683
- Gasser, T.C., Ogden, R.W., Holzapfel, G.A., 2006. Hyperelastic modelling of arterial layers with distributed collagen fibre orientations. *Journal of The Royal Society Interface* 3 (6), 15–35. doi:10.1098/rsif.2005.0073. ISSN 1742-5689.
- Ghassemieh, E., Nassehi, V., 2001. Stiffness analysis of polymeric composites using the finite element method. *Advances in Polymer Technology* 20 (1), 42–57. doi:10.1002/1098-2329(200121)20:1<42::AID-ADV1003>3.0.CO;2-F. ISSN 07306679
- Gladman, A.S., Matsumoto, E.A., Nuzzo, R.G., Mahadevan, L., Lewis, J.A., 2016. Biomimetic 4D printing. *Nature Materials* 15 (4), 413–418. doi:10.1038/nmat4544. ISSN 1476-1122
- Guo, Z., De Vita, R., 2009. Probabilistic constitute law for damage in ligaments. *Medical Engineering & Physics* 31, 1104–1109.
- Guo, Z., Sluys, L.J., 2006. Computational modelling of the stress-softening phenomenon of rubber-like materials under cyclic loading. *European Journal of Mechanics, A/Solids* 25 (6), 877–896. doi:10.1016/j.euromechsol.2006.05.011. ISSN 09977538
- Holzappel, G. A., Gasser, T. C., Ogden, R. W., 2000. A new constitutive framework for arterial wall mechanics and a comparative study of material models. *J. Elast.* 61, 1–48.
- Hull, D., Clyne, T.W., 1996. *An introduction to composite materials*, 2nd Cambridge University Press doi:10.1017/CBO9781139170130.
- Jensen, H.M., Christoffersen, J., 1997. Kink band formation in fiber reinforced materials. *Journal of the Mechanics and Physics of Solids* 45 (7), 1121–1136. doi:10.1016/S0022-5096(96)00126-3. ISSN 581 00225096
- Jiang, Y., Korpas, L.M., Raney, J.R., 2019. Bifurcation-based embodied logic and autonomous actuation. *Nat. Commun.* 10 (1). doi:10.1038/s41467-018-08055-3. ISSN 20411723
- Jiang, Y., Raney, J.R., 2019. 3D printing of amylopectin-based natural fiber composites. *Adv. Mater. Technol.* 4, 1900521.
- Kim, S.Y., Baines, R., Booth, J., Vasios, N., Bertoldi, K., Kramer-Bottiglio, R., 2019. Reconfigurable soft body trajectories using unidirectionally stretchable composite laminae. *Nature Communications* 10 (1), 3464. doi:10.1038/s41467-019-11294-7. ISSN 2041-1723
- Koh, C.T., Strange, D.G.T., Tonsomboon, K., Oyen, M.L., 2013. Failure mechanisms in fibrous scaffolds. *Acta Biomater.* 9, 7326–7334.
- Lees, J.K., 1968. A study of the tensile strength of short fiber reinforced plastics. *Polymer Engineering and Science* 8 (3), 195–201. doi:10.1002/pen.760080304. ISSN 0032-3888
- Lewis, J.A., 2006. Direct ink writing of 3d functional materials. *Adv. Funct. Mater.* 16, 2193–2204.
- Li, W., 2016. Damage Models for Soft Tissues: A Survey. *Journal of Medical and Biological Engineering* 36 (3), 285–307. doi:10.1007/s40846-016-0132-1. ISSN 21994757.
- López Jiménez, F., Kumar, S., Reis, P.M., 2016. Soft color composites with tunable optical transmittance. *Adv. Opt. Mater.* 4 (4), 620–626. doi:10.1002/adom.201500617.

- López Jiménez, F., Pellegrino, S., 2012. Constitutive modeling of fiber composites with a soft hyperelastic matrix. *International Journal of Solids and Structures* 49 (3), 635–647. doi:[10.1016/j.ijsolstr.2011.11.006](https://doi.org/10.1016/j.ijsolstr.2011.11.006). ISSN 0020-7683.
- Malek, S., Raney, J.R., Lewis, J.A., Gibson, L.J., 2017. Lightweight 3D cellular composites inspired by balsa. *Bioinspiration and Biomimetics* 12 (2), 1–11. doi:[10.1088/1748-3190/aa6028](https://doi.org/10.1088/1748-3190/aa6028). ISSN 17483190.
- Marini, G., Maier, A., Reeps, C., Eckstein, H.-H., Wall, W.A., Gee, M.W., 2012. A continuum description of the damage process in the arterial wall of abdominal aortic aneurysms. *International Journal for Numerical Methods in Biomedical Engineering* 28 (1), 87–99. doi:[10.1002/cnm.1472](https://doi.org/10.1002/cnm.1472). ISSN 20407939.
- Marklund, E., Varna, J., 2009. Modeling the effect of helical fiber structure on wood fiber composite elastic properties. *Applied Composite Materials* 16 (4), 245–262. doi:[10.1007/s10443-009-9091-9](https://doi.org/10.1007/s10443-009-9091-9). ISSN 0929189X.
- Melanitis, N., Galiotis, C., Tetlow, P.L., Davies, C.K., 1993. Monitoring the micromechanics of reinforcement in carbon fibre/epoxy resin systems. *Journal of Materials Science* 28 (6), 1648–1654. doi:[10.1007/BF00363362](https://doi.org/10.1007/BF00363362). ISSN 00222461.
- Merodio, J., Ogden, R.W., 2002. Material instabilities in fiber-reinforced nonlinearly elastic solids under plane deformation. *Archives of Mechanics* 54 (5–6), 525–552. ISSN 03732029.
- Merodio, J., Ogden, R.W., 2005. Mechanical response of fiber-reinforced incompressible non-linearly elastic solids. *International Journal of Non-Linear Mechanics* 40 (2–3), 213–227. doi:[10.1016/j.ijnonlinmec.2004.05.003](https://doi.org/10.1016/j.ijnonlinmec.2004.05.003). ISSN 00207462.
- Merodio, J., Ogden, R.W., 2005. On tensile instabilities and ellipticity loss in fiber-reinforced incompressible non-linearly elastic solids. *Mechanics Research Communications* 32 (3), 290–299. doi:[10.1016/j.mechrescom.2004.06.008](https://doi.org/10.1016/j.mechrescom.2004.06.008). ISSN 00936413.
- Mo, C., Kontsos, A., 2018. Twinning contributions to strain localizations in magnesium alloys. *Materials Science and Engineering A* 722, 206–215. doi:[10.1016/j.msea.2018.03.024](https://doi.org/10.1016/j.msea.2018.03.024). ISSN 09215093.
- Moran, P.M., Shih, C.F., 1998. Kink band propagation and broadening in ductile matrix fiber composites: Experiments and analysis. *International Journal of Solids and Structures* 35 (15), 1709–1722. doi:[10.1016/S0020-7683\(97\)00138-8](https://doi.org/10.1016/S0020-7683(97)00138-8). ISSN 00207683.
- Mullins, L., 1947. Effect of stretching on the properties of rubber. *J. Rubber Res.* 16, 275–289. ISSN 00207462.
- Ochiai, S., Hojo, M., Inoue, T., 1999. Shear-lag simulation of the progress of interfacial debonding in unidirectional composites. *Composites Science and Technology* 59 (1), 77–88. doi:[10.1016/S0266-3538\(98\)00054-2](https://doi.org/10.1016/S0266-3538(98)00054-2). ISSN 02663538.
- Ogden, R.W., Roxburgh, D.G., 1999. A pseudoelastic model for the Mullins effect in filled rubber. *Proceedings of the Royal Society of London. Series A: Mathematical, Physical and Engineering Sciences* 455 (1988), 28612877. doi:[10.1098/rspa.1999.0431](https://doi.org/10.1098/rspa.1999.0431). ISSN 00207462.
- Peña, E., 2011. Prediction of the softening and damage effects with permanent set in fibrous biological materials. *Journal of the Mechanics and Physics of Solids* 59, 1808–1822. doi:[10.1016/j.jmps.2011.05.013](https://doi.org/10.1016/j.jmps.2011.05.013). ISSN 00225096.
- Qi, H.J., Boyce, M.C., 2004. Constitutive model for stretch-induced softening of the stress-stretch behavior of elastomeric materials. *Journal of the Mechanics and Physics of Solids* 52 (10), 2187–2205. doi:[10.1016/j.jmps.2004.04.008](https://doi.org/10.1016/j.jmps.2004.04.008). ISSN 00225096.
- Qiu, G.Y., Pence, T.J., 1997. Loss of Ellipticity in Plane Deformation of a Simple Directionally Reinforced Incompressible Nonlinearly Elastic Solid. *Journal of Elasticity* 49 (1), 31–63. doi:[10.1023/A:1007441804480](https://doi.org/10.1023/A:1007441804480). ISSN 03743535.
- Qiu, G.Y., Pence, T.J., 1997. Remarks on the behavior of simple directionally reinforced incompressible nonlinearly elastic solids. *J Elast* 49 (1), 1–30. doi:[10.1023/A:1007410321319](https://doi.org/10.1023/A:1007410321319).
- Ranc, N., Wagner, D., 2005. Some aspects of Portevin-Le Chatelier plastic instabilities investigated by infrared pyrometry. *Materials Science and Engineering A* 394 (1–2), 87–95. doi:[10.1016/j.msea.2004.11.042](https://doi.org/10.1016/j.msea.2004.11.042). ISSN 09215093.
- Raney, J.R., Compton, B.G., Mueller, J., Ober, T.J., Shea, K., Lewis, J.A., 2018. Rotational 3D printing of damage-tolerant composites with programmable mechanics. *Proceedings of the National Academy of Sciences of the United States of America* (6) 1198–1203. doi:[10.1073/pnas.1715157115](https://doi.org/10.1073/pnas.1715157115). ISSN 1091-6490.
- Raney, J.R., Lewis, J.A., 2015. Printing mesoscale architectures. *MRS Bulletin* 40 (11), 943–950. doi:[10.1557/mrs.2015.235](https://doi.org/10.1557/mrs.2015.235). ISSN 0883-7694.
- Sacks, M.S., 2003. Incorporation of experimentally-derived orientation into a structural constitutive model for planar collagenous tissues. *Transactions of the ASME* 125, 280–287.
- Selezneva, M., Swolfs, Y., Katalagarianakis, A., Ichikawa, T., Hirano, N., Taketa, I., Karaki, T., Verpoest, I., Gorbatiikh, L., 2018. The brittle-to-ductile transition in tensile and impact behavior of hybrid carbon fibre/self-reinforced polypropylene composites. *Composites Part A: Applied Science and Manufacturing* 109, 20–30. doi:[10.1016/j.compositesa.2018.02.034](https://doi.org/10.1016/j.compositesa.2018.02.034). ISSN 1359835X.
- Simo, J.C., 1987. On a fully three-dimensional finite-strain viscoelastic damage model: Formulation and computational aspects. *Computer Methods in Applied Mechanics and Engineering* doi:[10.1016/0045-7825\(87\)90107-1](https://doi.org/10.1016/0045-7825(87)90107-1). ISSN 00457825.
- Triantafyllidis, N., Abeyaratne, R., 1983. Instabilities of a finitely deformed fiber-reinforced elastic material. *Journal of Applied Mechanics* 50 (1), 149. ISSN 00207462.
- Tsai, K.H., Kim, K.S., 1996. The micromechanics of fiber pull-out. *J Mech Phys Solids* 44 (7) 1147–1159, 1161–1177.
- Volokh, K., 2008. Prediction of arterial failure based on a microstructural bi-layer fibermatrix model with softening. *Journal of Biomechanics* 41 (2), 447–453. doi:[10.1016/j.jbiomech.2007.08.001](https://doi.org/10.1016/j.jbiomech.2007.08.001). ISSN 0021-9290.
- Weaver, J.C., Milliron, G.W., Miserez, A., Evans-Lutterodt, K., Herrera, S., Gallana, I., Mershon, W.J., Swanson, B., Zavattieri, P., DiMasi, E., Kisailus, D., 2012. The stomatopod dactyl club: a formidable damage-tolerant biological hammer. *Science* 336 (6086), 1275–1280. doi:[10.1126/science.1218764](https://doi.org/10.1126/science.1218764).
- Yang, W., Sherman, V.R., Gludovatz, B., Schaible, E., Stewart, P., Ritchie, R.O., Meyers, M.A., 2015. On the tear resistance of skin. *Nat Commun* 6, 1–10. doi:[10.1038/ncomms7649](https://doi.org/10.1038/ncomms7649).
- Yilmaz, A., 2011. The portevin-Le chatelier effect: a review of experimental findings. *Sci Technol Adv Mater* 12 (6). doi:[10.1088/1468-6996/12/6/063001](https://doi.org/10.1088/1468-6996/12/6/063001).
- Zavattieri, P.D., Savic, V., Hector, L.G., Fekete, J.R., Tong, W., Xuan, Y., 2009. Spatio-temporal characteristics of the Portevin-Le Chatelier effect in austenitic steel with twinning induced plasticity. *International Journal of Plasticity* 25 (12), 2298–2330. doi:[10.1016/j.ijplas.2009.02.008](https://doi.org/10.1016/j.ijplas.2009.02.008). ISSN 00207462.
- Zhong, W., Li, F., Zhang, Z., Song, L., Li, Z., 2001. Short fiber reinforced composites for fused deposition modeling. *Materials Science and Engineering A* 301 (2), 125–130. doi:[10.1016/S0921-5093\(00\)01810-4](https://doi.org/10.1016/S0921-5093(00)01810-4). ISSN 07496419.